Dalton Transactions

ROYAL SOCIETY OF CHEMISTRY

PAPER

View Article Online
View Journal | View Issue

Cite this: *Dalton Trans.*, 2025, **54**, 17458

Researching advancements in the electrochemical performance of molybdenum-based spherical polyoxometalate/reduced graphene oxide aerogel composites as electrode materials for supercapacitors

Renyou Huang, Jihua Wang, * Junwang Liu, Xiaoyan Cai, Lige Gong and Limin Dong

A composite aerogel formed using spherical polyoxometalate {Mo_{132}} and graphene exhibits characteristics distinct from those of other aerogels. It retains the three-dimensional mesoporous channels typical of graphene aerogels and incorporates {Mo_{132}}-derived micropores. These structural features together furnish additional ion-transport channels for conductive particles. This aerogel material showcases a substantial specific surface area (207.114 $m^2\ g^{-1}$), which is significantly higher than the of pure graphene aerogel (96.327 $m^2\ g^{-1}$), indicating that the material has a rich microporous structure. The existence of {Mo_{132}} reduced the charge transfer resistance R_{ct} of the material to varying degrees, reaching a minimum of 1.916 Ω, far lower than the 2.861 Ω of the pure graphene aerogel, which further explains the role of mesopores. At a current density of 10 A g^{-1} and after 10 000 cycles, the Coulomb efficiency of the material remained at 77.97%. A symmetrical supercapacitor is made of this aerogel material, with a specific capacitance of 100.6 F g^{-1} at a current density of 1 A g^{-1}. The energy density at a current density of 10 A g^{-1} is approximately 13 Wh kg^{-1}, and the power density is approximately 7500 W kg^{-1}. The data suggest that the multi-stage pore structure of the new aerogel can not only provide high-density active sites and increase charge storage, but also reduce internal charge-transfer resistance and improve power density and cycling stability. This study presents a novel approach for exploring electrode materials for supercapacitors.

Received 2nd September 2025,
Accepted 27th October 2025

DOI: 10.1039/d5dt02107c

rsc.li/dalton

1. Introduction

As a green energy storage device, supercapacitors (SCs) have the advantages of high power density, rapid charging/discharging capabilities, long cycle life and excellent safety performance.[1–3] The electrode material is an important factor in determining the performance of supercapacitors. Consequently, developing stable green electrode materials with high capacitance, energy density and power density is important to obtain high-performance supercapacitors. Traditional electrode materials mainly have two mechanisms of action, namely double-layer capacitance (EDLC) and pseudocapacitance (PC). The electrode materials for double-layer capacitors are mainly carbon materials, such as graphene,[4,5] carbon nanotubes,[6,7] activated carbon[8,9]and so on. Pseudocapacitive electrode materials mainly include transition metal oxides, such as ruthenium oxide,[10,11] nickel oxide,[12,13] and manganese dioxide,[14,15] as well as conductive polymers[16] such as polypyrrole,[17,18] polyaniline,[19,20] and polythiophene.[21,22]

Two-dimensional graphene materials have a large specific surface area and good conductivity, which have been widely used as electrode materials,[23–26] However, their propensity to agglomerate easily restricts the electrochemical performance of graphene materials and impacts their application.[27,28] Graphene sheets can be induced to overlap with each other, so these sheets can self-assemble into graphene aerogels. The formation of aerogels can not only effectively prevent the agglomeration of lamellar graphene but also facilitate an increase in the specific surface area.[29,30] Graphene aerogels have a three-dimensional network structure, good conductivity, and a large porosity and specific surface area. These characteristics make them a viable electrode material option for supercapacitors.[31–34]

Polyoxometalates (POMs) are metal oxygen cluster compounds formed by coordinating high oxidation state transition

School of Materials Science and Chemical Engineering, Harbin University of Science and Technology, Heilongjiang 150040, China. E-mail: wjh99924@hrbust.edu.cn

metal ions with oxygen atoms according to a certain structure. POMs have high redox stability and exhibit pseudocapacitive electrochemical behavior, making them an ideal energy storage material.[35–37] In recent years, numerous studies in the literature have focused on coordination polymers or complexes constructed from different types of polyoxometalates (POMs). For instance, Keggin-type ($[HPMo_{12}O_{40}]^{2-}$ and $[PMo_{12}O_{40}]^{3-}$),[38,39] Wells–Dawson-type ($[P_2W_{18}O_{62}]^{6-}$),[40] and organophosphorus Strandberg-type ($[(C_6H_5PO_3)_2Mo_5O_{15}]$)[41] POMs serve as building units to form coordination polymers or nanocage-cluster frameworks with metals such as Cu and Ag, along with organic ligands. When utilized in supercapacitors, these materials uniformly demonstrate outstanding performance, thus further augmenting their potential applications within the energy-storage domains.

The electrode material should have high capacity, high rate capability, and excellent cycling stability. However, it is challenging for a single-component electrode material to satisfy these requirements concurrently. Consequently, multiple components are frequently employed to construct composite systems, leveraging the synergistic effects among the components to obtain electrode materials with multiple excellent properties coexisting.[42–46] The effective combination of the two materials can preserve the excellent electrical conductivity and chemical stability of carbon materials and the high specific capacitance and energy density characteristics of POMs. Moreover, the synergistic interaction of multiple components addresses the issues of low bandgap and poor conductivity of pseudocapacitive materials, thereby improving the capacitance of electrode materials.[47–52] Polyoxometalate $\{Mo_{132}\}$ consists of 12 pentagonal $\{Mo_6^{VI}\}$ units and 30 $\{Mo_2^{V}\}$ units (Fig. 1). Owing to the symmetrical icosahedral structure of this spherical molecule, which bears a resemblance to the cosmic model described by Kepler, $\{Mo_{132}\}$ is also referred to as "keplerates". Polyoxometalates possess the ability to store electrons while also exhibiting a nanoporous structure.[53–55] The presence of micropores with a diameter of 3.2 Å can enhance the material's specific surface area and increase the number of active sites. So in this paper, a molybdenum-based spherical POM cluster $\{Mo_{132}\}$ and graphene are combined to form three-dimensional porous aerogel electrode materials *via* the hydrothermal method, and their electrochemical properties are analyzed and discussed.

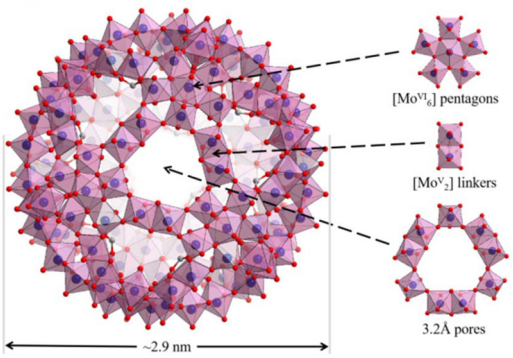

Fig. 1 Structural diagram of Mo_{132}.

2. Materials and methods

2.1. Materials

Hydrazine sulfate ($N_2H_4{\cdot}H_2SO_4$), ammonium molybdate tetrahydrate ($(NH_4)_6Mo_7O_{24}{\cdot}4H_2O$), ammonium acetate ($CH_3COONH_4$), glacial acetic acid ($CH_3COOH$) and sodium nitrate ($Na_2NO_3$) were purchased from Tianjin Zhonglian Chemical Co., Ltd. Graphite powder was purchased from Tianjin Hongwu Materials Technology Co., Ltd. Sulfuric acid, hydrochloric acid, potassium permanganate ($KMnO_4$), hydrogen peroxide (H_2O_2), polyvinylidene fluoride (PVDF) and *N*-methylpyrrolidone (NMP) were purchased from Tianjing Fuyu Fine Chemicals Co., Ltd.

2.2. Preparation of GO

A mixture of graphite powder (3 g), sodium nitrate (1.5 g) and concentrated sulfuric acid (69 mL) was immersed in an ice-water bath for 30 minutes. Potassium permanganate (9 g) was gradually added to the above solution. After 30 minutes, the solution turned green. Then deionized water (250 mL) was added and stirred for 20 minutes. Then, hydrogen peroxide (45 mL) was added and stirred for 20 minutes. The product was washed with deionized water until the solution reaches a neutral pH. After centrifugation, the product was dried in an oven for 24 hours to obtain graphene oxide (GO).

2.3. Preparation of the POM cluster $\{Mo_{132}\}$

The synthesis of $\{Mo_{132}\}$ was adapted from a previous report.[53] Briefly, hydrazine sulfate (0.8 g) was added to a solution of ammonium molybdate tetrahydrate (5.6 g) and ammonium acetate (12.5 g) in deionized water (250 mL). The solution was stirred for 10 minutes and glacial acetic acid (50%, 83 mL) was added. After 4 days, reddish-brown crystals were obtained and washed with 90% ethanol. After drying, the final product obtained was $\{Mo_{132}\}$ crystals.

2.4 Synthesis of $\{Mo_{132}\}$/rGA composites

GO (30 mg) was dispersed in deionized water (15 mL) and ultrasonic dispersion was performed for 15 minutes to prepare a graphene suspension (2 mg mL^{-1}). Then 7.5 mg, 5 mg, and 3.75 mg of $\{Mo_{132}\}$ were added to the graphene suspension, respectively (corresponding to the $\{Mo_{132}\}$: GO ratios of 1 : 4, 1 : 6, and 1 : 8). The solution was dispersed using ultrasound for 15 minutes. Then, the mixture was placed into a Teflon-lined autoclave and maintained at 180 °C for 24 h to form a reduced graphene oxide hydrogel. Finally, the synthesized $\{Mo_{132}\}$/rGA hydrogel was freeze-dried at −48 °C for 48 hours to obtain a $\{Mo_{132}\}$/rGA aerogel. Based on the ratios of $\{Mo_{132}\}$ to GO, the resulting composite materials are named $\{Mo_{132}\}$/rGA-4, $\{Mo_{132}\}$/rGA-6, and $\{Mo_{132}\}$/rGA-8, respectively.

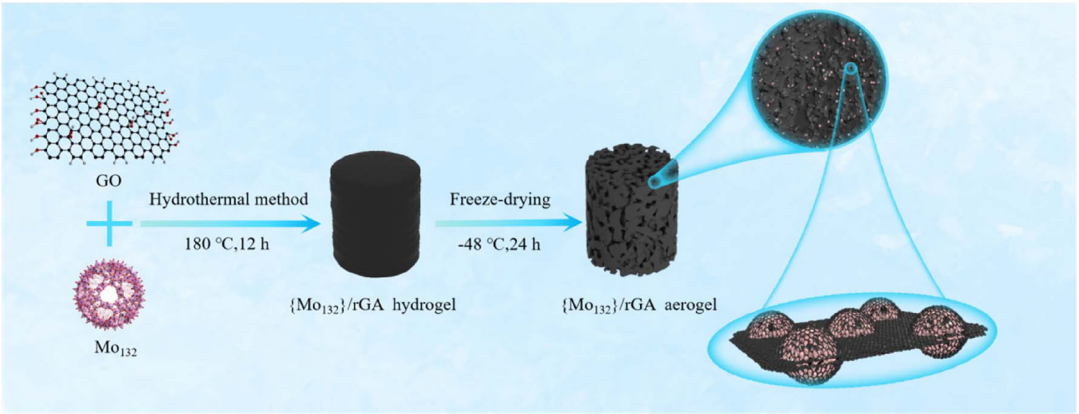

Fig. 2 Preparation process diagram of $\{Mo_{132}\}$/rGA composites.

Additionally, a pure reduced graphene oxide aerogel was prepared and named rGA (Fig. 2).

2.5 Calculation formula

The specific capacitance of electrodes was calculated from the charge/discharge curves using the following equation:

$$C = \frac{I \times \Delta t}{m \times \Delta V} \quad (1)$$

where C (F g^{-1}) is the specific capacitance based on the mass of active carbons, I (A) and Δt are the constant charge/discharge current and discharge time measured in seconds, and m (g) and ΔV (V) are the mass of active materials and the potential window, respectively.

The energy density (E) and power density (P) were calculated using the following equations:

$$E = \frac{1}{2} \times C \times V^2 \quad (2)$$

$$P = \frac{E}{\Delta t} \quad (3)$$

The ion diffusion coefficient was calculated according to the equation:

$$i(\nu) = a \times \nu^b \quad (4)$$

$$i(V) = k_1\nu + k_2\nu^{1/2} \quad (5)$$

where i is the current density, ν and V are the scanning rate and potential, and b is an important metric to evaluate the charge-storage kinetics. Also, $k_1\nu$ and $k_2\nu^{1/2}$ represent the surface-controlled and diffusion-controlled processes, respectively.

2.6 Material characterization

X-ray diffraction (XRD) was performed using a D/max-γB X-ray diffractometer from Rigaku Corporation, Japan. The characterization parameters included copper target Kα radiation with a wavelength of 0.154 nm and a scanning angle 2θ range of 5–90°. The structural features and functional groups of the system were analyzed by Fourier Transform Infrared (FTIR) spectroscopy using an ALPHA II Fourier transform infrared spectrometer from Bruker Corporation, Germany. An ESCALAB Xi+ X-ray photoelectron spectrometer manufactured by Thermo Fisher Scientific was used to test the binding form and valence state changes of materials. The samples were characterized within a wavenumber range of 500–4000 cm^{-1}. The morphological structure of the cross-sectional surface of the sample was observed using a scanning electron microscope (SEM, FEI Sirion-200). The operating voltage was set at 10 kV. The specific surface area was measured using an Autosorb IQ instrument from Quantachrome Instruments, USA. The sample was degassed at 60 °C for 6 hours. Measurements were conducted in full-pore analysis mode under a nitrogen atmosphere.

2.7 Preparation of electrodes and electrochemical measurements

$\{Mo_{132}\}$/rGA (8 mg) was mixed with conductive carbon black (1 mg), and then polyvinylidene fluoride (1 mg) was added and ground evenly. *N*-Methylpyrrolidone (NMP, 60 μL) was dropped into the mixed powder to obtain a viscous slurry. The slurry was spread evenly onto a prepared nickel foam sheet (1 cm × 1 cm) and vacuum dried in an oven at 60 °C for 24 hours. After drying, a pressure of 10 MPa was applied to the nickel sheet for about 10 seconds to obtain the working electrode ready for use.

A three-electrode cell system was set up to assess the electrochemical performance using an electrochemical workstation CH700E. The potentials and current were measured concerning the mercury oxide electrode as a reference electrode. Platinum wire and nickel foam with active materials were used as the counter and working electrode, respectively. The electrochemical performance was evaluated by testing using cyclic voltammetry (CV), constant current charge discharge (GCD), alternating current impedance (EIS), and cycling stability in the electrolyte solution (0.5 M KOH). Cyclic voltammetry measurements were performed at various scan rates in a potential range from −1 to 0 V.

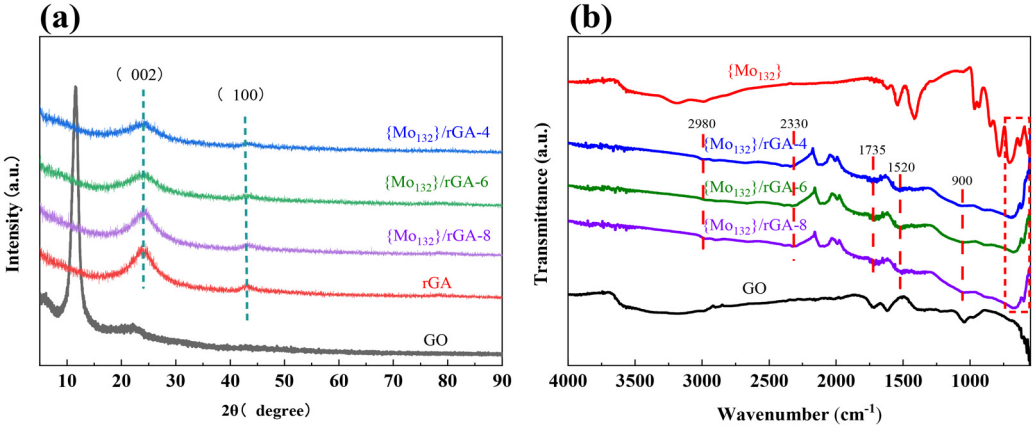

Fig. 3 (a) XRD patterns of the composite materials with different ratios. (b) FTIR spectra of the composite materials with different ratios.

3. Results and discussion

It can be observed from Fig. 3(a) that the characteristic diffraction peak of GO is located at approximately $2\theta = 11.3°$, corresponding to the (001) crystal plane. The diffraction peak is associated with an increase in interlayer spacing. This indicates that the formation of GO is mainly attributed to the introduction of oxygen-containing groups into the interlayer spacing during the oxidation process, which leads to structural expansion. After undergoing a hydrothermal reaction, two weak and broad diffraction peaks were observed at around $2\theta = 24°$ and 43° in the {Mo_{132}}/rGA-4, and {Mo_{132}}/rGA-6 and {Mo_{132}}/rGA-8 samples, corresponding to the (002) and (100) lattice planes of graphite-like crystallites. The XRD patterns confirmed that GO undergoes deoxygenation during hydrothermal reduction to form reduced graphene oxide.

As shown Fig. 3(b), the hydroxyl group in GO has a characteristic peak at 3400–3200 cm^{-1}, and the three composite systems in the figure do not exhibit a distinct peak at this wavelength, suggesting that the hydroxyl group has been reduced and removed. A weak peak emerges at 2980 cm^{-1} (refer to the long dashed line), which mainly corresponds to the absorption peak of the alkyl group generated after reduction. The curves of the three systems all display weak peaks near a wavelength of 2330 cm^{-1}, close to the absorption peak of CO_2. It is likely that the CO_2 in the environment was not completely discharged during the testing process, resulting in interference peaks. The stretching vibration peaks of carboxylic acid groups (–COOH) and carbonyl groups (C═O) at 1735 cm^{-1} (refer to the long dashed line) show a decrease in or even disappearance of intensity after reduction, indicating that carboxylic acid groups have been reduced to other structures (such as alkyl or vinyl). Similarly, a strong peak appears at 1520 cm^{-1} (refer to the long dashed line), corresponding to the absorption peak of the alkyl functional group generated after reduction, and its peak intensity is related to the reduction conditions. The strong absorption peak at 970 cm^{-1} corresponds to the stretching vibration mode of the molybdenum–oxo double bond (Mo═O). The characteristic peaks of {Mo_{132}} are mainly distributed in the region below 900 cm^{-1}. The three {Mo_{132}}/rGA composites also exhibit a series of characteristic peaks corresponding to {Mo_{132}} at approximately 600 cm^{-1}, indicating successful composite formation between {Mo_{132}} and rGA (refer to the dotted box).

X-ray photoelectron spectroscopy (XPS) tests were performed on the {Mo_{132}}/rGA-6 electrode both before and after cycling. Fig. 4(b) presents the high-resolution spectrum of C 1s, with peaks corresponding to C═O (288.8 eV), C–O (286.0 eV), and C–C bonds (284.8 eV). A π–π* shake-up satellite peak emerged at 290.75 eV, suggesting a high degree of graphitization and efficient charge transfer. Fig. 4(c) shows two pairs of Gaussian peaks in the high-resolution spectrum of Mo 3d at binding energies of 236.2 eV and 232.7 eV, corresponding to Mo $3d_{3/2}$ and Mo $3d_{5/2}$, respectively. This indicates that Mo is in the VI oxidation state. When comparing the C 1s high-resolution spectra of the {Mo_{132}}/rGA-6 electrode before and after cycling (Fig. 4(b) and (e)), no significant differences were observed in the C 1s spectra. This implies that the rGA skeleton remained intact and there was no element loss. In comparison with the high-resolution spectra of Mo 3d (Fig. 4(c) and (f)), no significant peak position shift was detected. It can be inferred that the {Mo_{132}}/rGA-6 electrode material demonstrates excellent cycling stability.

As shown in Fig. 5(a), a small number of graphene flakes are distributed in the system (see the circled area), and granular polyacids cover the surfaces of the layers, while the majority of the graphene is in the form of curled flakes. Additionally, numerous large holes in the architecture penetrate the entire system. Due to the large size of the holes (as shown by the straight line in the figure), the walls between the holes are thin, making it difficult to form a complete hole wall. As shown in Fig. 5(b), with an increase in graphene content, the number of layered graphene sheets in the system increases, the pore size significantly decreases, the number of pore walls increases, and the thickness increases. As shown in Fig. 5(c), as the graphene content further increases, the phenomenon of

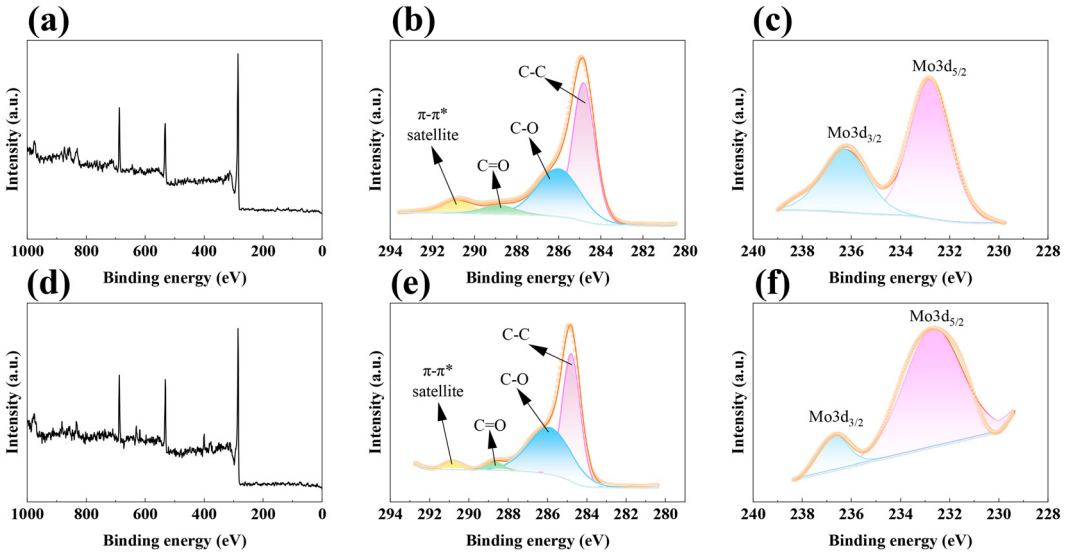

Fig. 4 (a and d) Full XPS spectra of the {Mo_{132}}/rGA-6 electrode samples before and after cycling; (b and e) C 1s XPS peaks of the {Mo_{132}}/rGA-6 electrode samples before and after cycling; and (c and f) Mo 3d XPS peaks of the {Mo_{132}}/rGA-6 electrode samples before and after cycling, respectively.

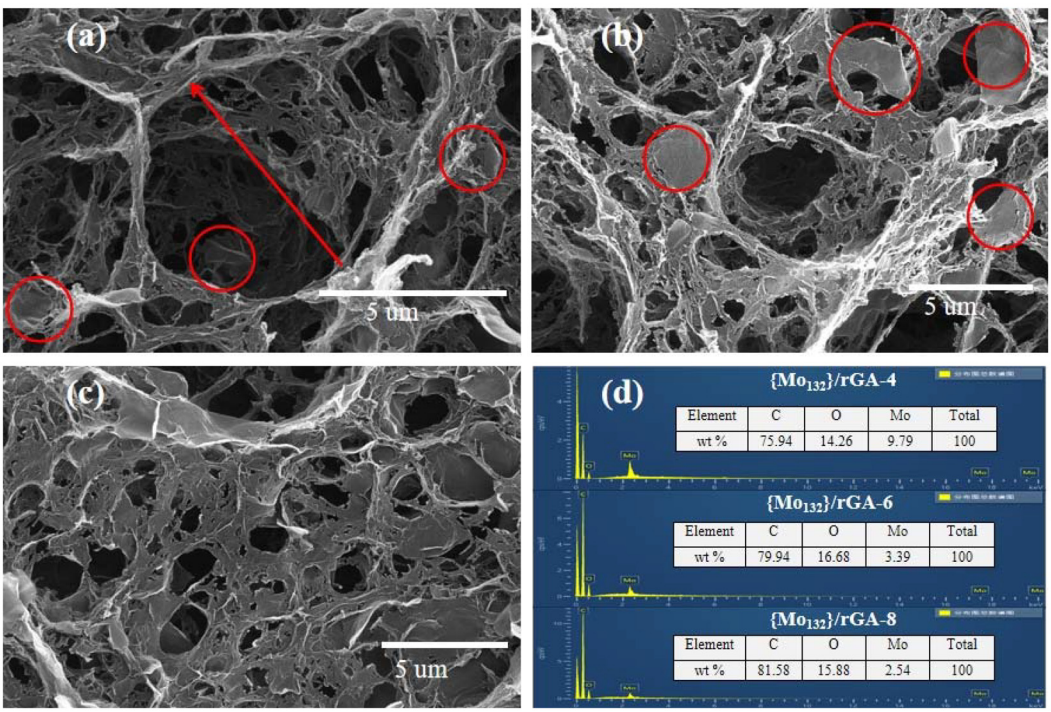

Fig. 5 SEM images of the composite materials with different ratios of {Mo_{132}} and rGA. (a) {Mo_{132}}/rGA-4; (b) {Mo_{132}}/rGA-6; (c) {Mo_{132}}/rGA-8; and (d) element proportion.

layer overlap becomes more pronounced, resulting in a decrease in the number of pores in the system, a significant reduction in pore size, a weakening of spatial penetration, and a more tightly-packed composition structure. As demonstrated in Fig. 5(d), as the GO content gradually increases, the Mo content gradually decreases.

As shown in Fig. 6(a), the adsorption–desorption curves of the four systems exhibit similar shapes, characterized by type IV isotherms and H3 hysteresis loops, indicating the presence of numerous mesopores in the material. The red curve lies slightly higher than the other curves at lower relative pressures, indicating a certain number of micropores in the {Mo_{132}}/

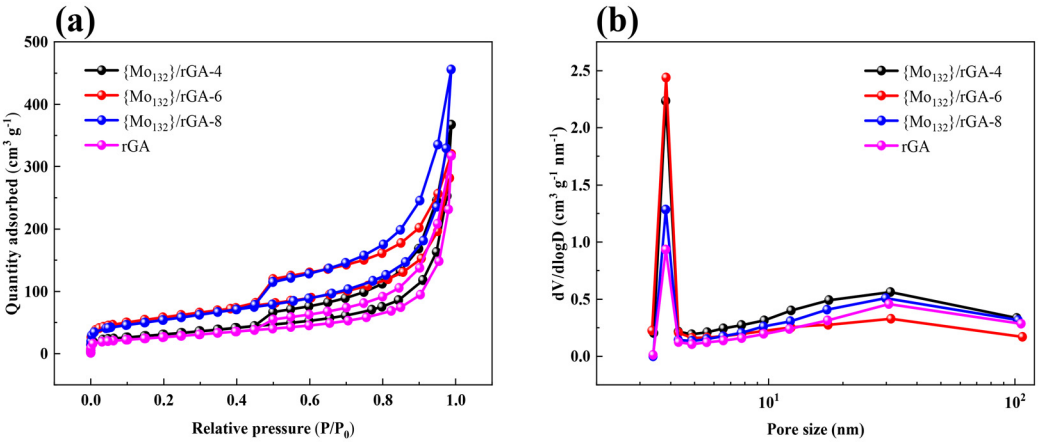

Fig. 6 (a) Adsorption–desorption isotherms and (b) pore size distribution of the composite materials with different ratios.

rGA-6 system, which exhibits nitrogen absorption at low relative pressures. Fig. 6(b) shows an analysis diagram of pore size distribution, where the ordinate represents the rate of change in pore volume with respect to the logarithm of pore size. At a pore size of 2 nm, the curve peak of the $\{Mo_{132}\}$/rGA-6 system is the highest, indicating that this sample has the highest number of micropores. Through calculation, the micropore areas of $\{Mo_{132}\}$/rGA-4, $\{Mo_{132}\}$/rGA-6, $\{Mo_{132}\}$/rGA-8, and pure rGA are 14.048, 47.390, 1.258, and 2.759 $m^2\ g^{-1}$, respectively. The figures show that the mesopore distributions of the four systems are relatively similar, with no significant disparities. However, the $\{Mo_{132}\}$/rGA-6 system has the largest micropore area, resulting in the highest specific surface area of 207.114 $m^2\ g^{-1}$, while the specific surface areas of the other three systems are 193.956, 112.198, and 96.327 $m^2\ g^{-1}$, respectively. This outcome is in agreement with the conclusions obtained from the analysis of the scanning images.

As illustrated in Fig. 7, the cyclic voltammetry (CV) curves exhibit a morphological transition from rectangular-like profiles to spindle-shaped configurations with increasing scan

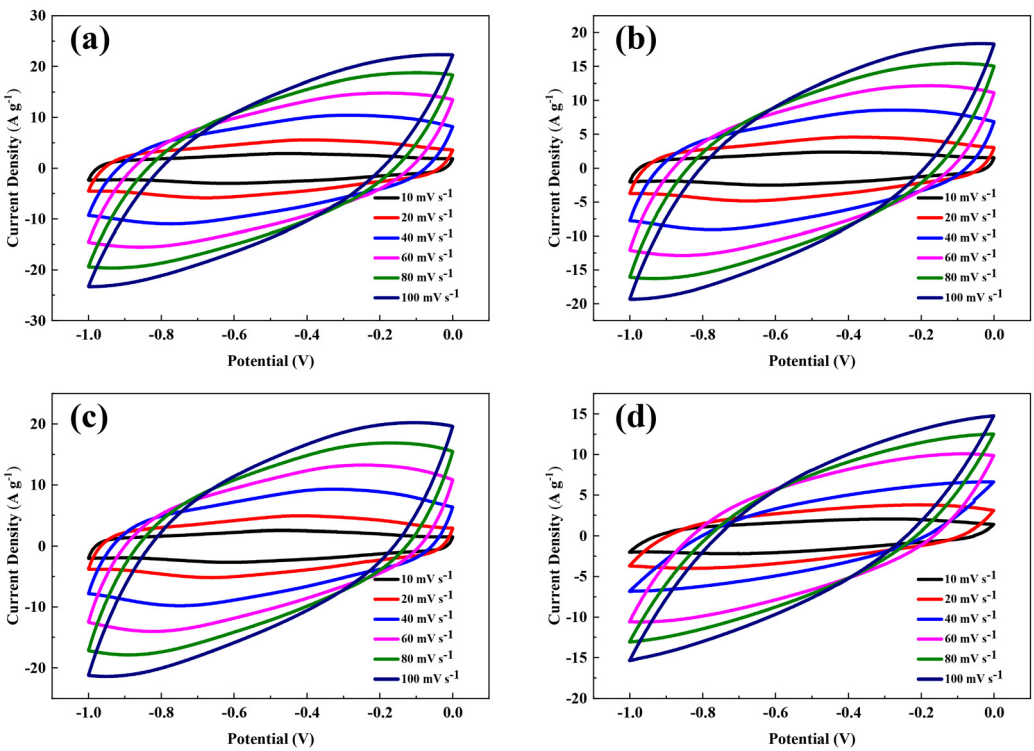

Fig. 7 CV curves of various systems with different ratios of $\{Mo_{132}\}$ and rGA. (a) $\{Mo_{132}\}$/rGA-4; (b) $\{Mo_{132}\}$/rGA-6; (c) $\{Mo_{132}\}$/rGA-8; and (d) pure rGA.

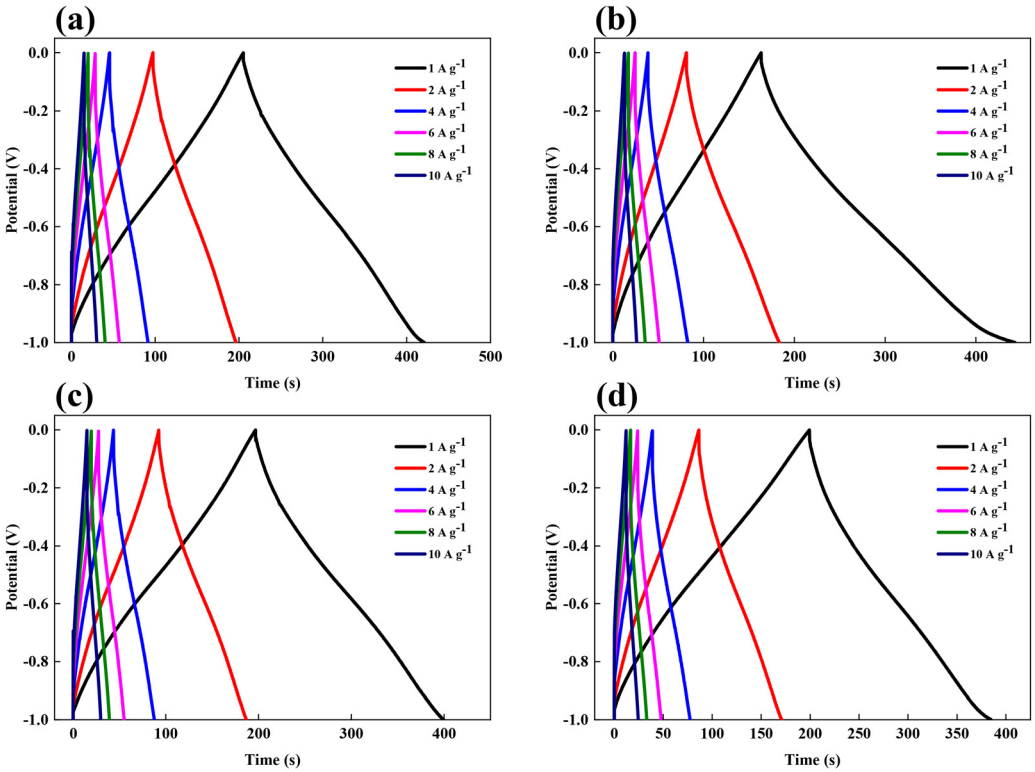

Fig. 8 GCD curves of various systems with different ratios of {Mo_{132}} and rGA. (a) {Mo_{132}}/rGA-4; (b) {Mo_{132}}/rGA-6; (c) {Mo_{132}}/rGA-8; and (d) pure rGA.

rates, which strongly indicates the predominance of an electric double-layer capacitive (EDLC) mechanism. The progressive enlargement of the CV integrated area at higher scan rates is attributed to decreased diffusion layer thickness. This reduction induces an accumulation of electroactive species at the electrode surface, thereby amplifying the interfacial concentration gradient. Consequently, the intensified mass transport kinetics enhance the current response, which is manifested as expanded CV curve areas. Calculation results show that the ratios of the oxidation peak current to the reduction peak current under different conditions are 0.956, 0.949, 0.944, and 0.961, all approaching 1.0. Additionally, the symmetry observed in the cyclic voltammograms across varying scan rates suggests that the reaction demonstrates a certain degree of reversibility.

As depicted in Fig. 8, almost all the galvanostatic charge–discharge (GCD) curves at different current densities exhibit an isosceles triangular shape. The slopes of the charge–discharge curves for each set of samples are essentially equivalent, with no apparent plateaus, indicating that charge storage is predominantly governed by physical adsorption and encompasses rapid ion adsorption–desorption processes. The electron transfer between Mo_{132} and rGA takes place through the Mo^{5+}/Mo^{6+} redox active site, in combination with the two-dimensional conjugated structure of rGA and the electron transfer characteristics of the π-electron cloud. The two substances interact with one another, and the valence state cycling of Mo^{5+}/Mo^{6+} in Mo_{132} brings about electron storage and release. After electrons transfer to rGA *via* Mo_{132}, they are rapidly transferred through its π-bond network. The mass-specific capacitance of each electrode material can be calculated using formula (1). The mass-specific capacitances of {Mo_{132}}/rGA-4, {Mo_{132}}/rGA-6, {Mo_{132}}/rGA-8, and rGA are 215.7 F g^{-1}, 279.8 F g^{-1}, 202.7 F g^{-1}, and 185.4 F g^{-1}, respectively. This indicates that {Mo_{132}}, acting as a pseudocapacitive component, significantly contributes to the enhancement of electrode performance. Table 1 demonstrates that the incorporation of {Mo_{132}} improves the performance of supercapacitor electrode materials.

Table 1 Summary table of rGO as a supercapacitor electrode material

Electrode	Electrolyte	Current density (A g^{-1})	C_{sp} (F g^{-1})	Ref.
Co-POM/GO	1 M H_2SO_4	0.5	211.3	56
HPW/rGO	5 M H_2SO_4	0.5	156.9	57
MOF@3D GO	6 M KOH	0.5	214	58
rGO/Ppy/Zn-MOF	6 M KOH	1	175	59
MOF 5-GO	6 M KOH	3	180.45	60
SN-GA	6 M KOH	1	244	61
PANI/GO/Cr-MOF	2 M $HClO_4$	0.5	243.125	62
{Mo_{132}}/rGA	0.5 M KOH	1	279.8	This work

To deeply explore the kinetic characteristics of the {Mo_{132}}/rGA-6 electrode, based on the cyclic voltammetry (CV) curve,

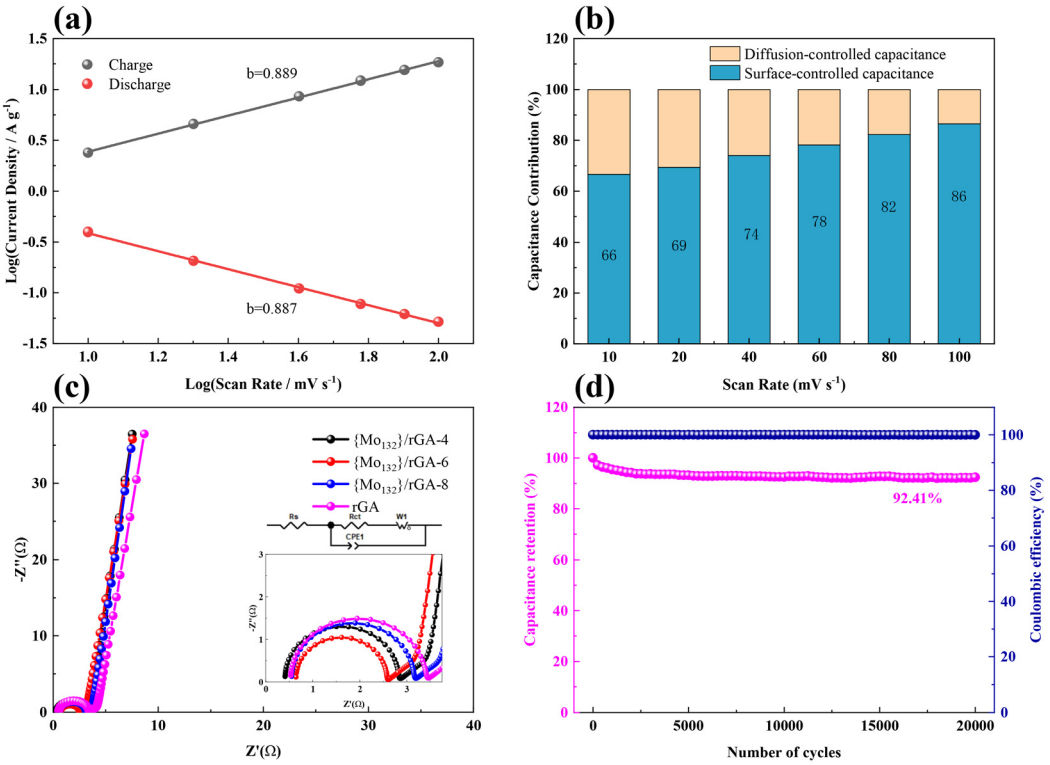

Fig. 9 (a) Linear plot of log *i* *versus* log *v* obtained from CV curves; (b) the surface-controlled and diffusion-controlled contribution ratios at different scan rates during CV processes; (c) Nyquist plot; and (d) cycling performance of various systems at a current density of 10 A g^{-1}.

the contribution rates of surface control and diffusion control were calculated using the formula described in the Materials and methods section. The values typically range between 0.5 and 1. When the *b* value is 0.5, it indicates that the battery exhibits slow kinetic characteristics, whereas when the *b* value is 1, it indicates that the capacitor possesses ideal fast kinetic behavior. In Fig. 9(a), for the {Mo_{132}}/rGA-6 electrode, the calculated *b* value is approximately 0.889, indicating that its charging and discharging processes are simultaneously influenced by both surface control and diffusion control. However, since this *b* value is closer to 1, it is clear that surface control behavior predominates. In Fig. 9(b), the blue bars represent the surface-controlled capacitance, while the orange bars represent the diffusion-controlled capacitance. As the scan rate increases, the surface-controlled capacitance increases from 66% to 86%, whereas the diffusion-controlled capacitance decreases from 34% to 14%. This indicates that the energy storage of the sample primarily relies on the rapid charge adsorption–desorption mechanism on the surface. At a high scan rate of 100 mV s^{-1}, the specific capacitance of the surface-controlled capacitance remains relatively high, and the decrease in the specific capacitance of the diffusion-controlled capacitance is gradual. This indicates that the material possesses both rapid charge transfer and ion diffusion capabilities, making it suitable for high-power applications.

Fig. 9(c) depicts the Nyquist plots of various systems tested at frequencies ranging from 0.01 Hz to 100 kHz. The Nyquist plot provides insights into the impedance characteristics and interfacial electrochemical behaviors of these systems. At low frequencies, the curves exhibit a linear trend, while at high frequencies, they form a semicircular shape. The inset reveals that all samples exhibit a standard and well-defined semicircular shape at high frequencies, indicating that they have a uniform and stable interface. Among these, the red curve has the smallest radius, while the pink curve has the largest radius. The diameter of the semicircle corresponds to the charge transfer resistance (R_{ct}). The charge-transfer resistances of {Mo_{132}}/rGA-4, {Mo_{132}}/rGA-6, {Mo_{132}}/rGA-8, and pure rGA are 2.385 Ω, 1.916 Ω, 2.578 Ω and 2.861 Ω, respectively. A smaller radius implies a lower charge transfer resistance, facilitating easier charge transfer and better conductivity. This implies that the {Mo_{132}}/rGA-6 system exhibits the best conductivity. At low frequencies, all curves indicate an almost vertical linear trend. The inset further indicates that the red curve has the steepest slope at low frequencies, demonstrating that the {Mo_{132}}/rGA-6 system exhibits the most pronounced capacitive behavior. The previous characterization and performance testing results show that {Mo_{132}}/rGA-6 has certain advantages over other groups. Consequently, its cyclic stability was tested, as shown in Fig. 9(d). After 20 000 cycles, the {Mo_{132}}/rGA-6 achieves a coulombic efficiency of 92.41%, approaching 100%, with minimal fluctuations. This demonstrates its high electrochemical stability, making it suitable for applications requiring long-term durability.

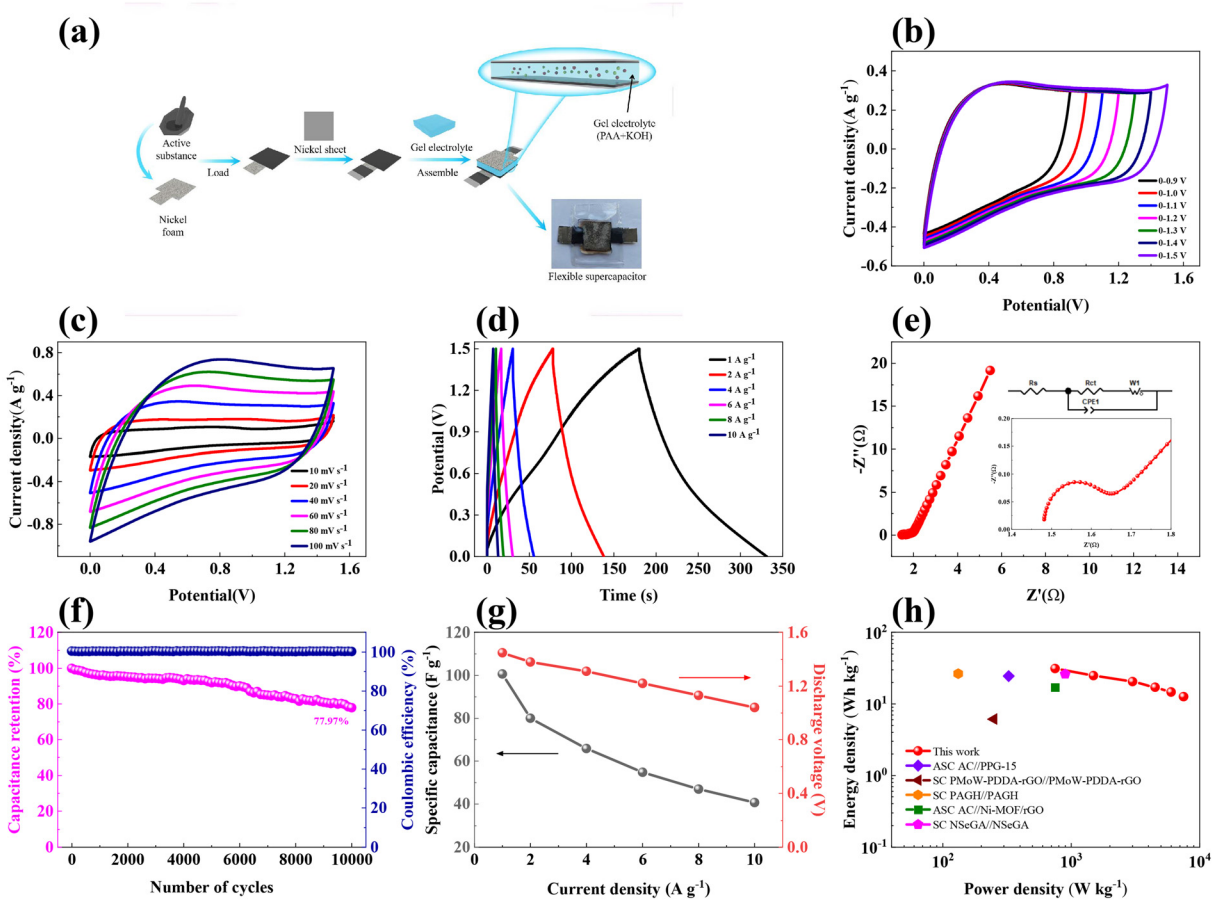

Fig. 10 Electrochemical performance of the capacitive symmetric device. (a) Schematic illustration of $\{Mo_{132}\}$/rGA-6//$\{Mo_{132}\}$/rGA-6. (b) CV curves of the device in different voltage windows. (c) CV curves of the device at different scan rates. (d) GCD curves of the device at different current densities. (e) Nyquist plot. (f) Cycling performance of the device at 10 A g^{-1}. (g) Plots of specific capacitance and discharge voltage *versus* current density. (h) Ragone plot in comparison with the literature.

A symmetric capacitive device was assembled using $\{Mo_{132}\}$/rGA-6 as both the cathode and anode. Fig. 10(b) displays the CV curves of the symmetric device in different voltage windows. These curves exhibit quasi-rectangular closed loops formed by forward and reverse scans with a slight tilt, reflecting the characteristics of a hybrid energy storage mechanism. Fig. 10(c) presents the CV curves at various scan rates, showing no distinct redox peaks, which indicates the dominant role of electric double-layer capacitance (EDLC). Minor elliptical distortion suggests the presence of certain pseudocapacitive behavior. The high symmetry between forward and reverse scans demonstrates excellent reversibility of the device. As shown in Fig. 10(d), the GCD curve exhibits nonlinear characteristics, which are consistent with the pseudocapacitive properties of the material. As shown in Fig. 10(e), the device exhibits a distinct semicircular arc in the high-frequency region, indicating the presence of a certain charge transfer resistance. Meanwhile, a clear linear curve is observed in the low-frequency region, suggesting the existence of charge diffusion behavior. The equivalent circuit in the inset diagram includes the solution resistance (R_s), charge transfer resistance (R_{ct}), constant phase element (CPE), and Warburg impedance (w_1). These parameters enable quantitative analysis of the reaction kinetics of the electrode, interfacial properties, and mass transport limitations. The device demonstrates a capacitance retention rate of 77.97% after 10 000 cycles at a current density of 10 A g^{-1} (Fig. 10(f)). The coulombic efficiency of the device is nearly 100%. The device exhibits a specific capacitance of 100.6 F g^{-1} at a current density of 1 A g^{-1}. Moreover, it exhibits only a minor voltage drop of 0.149 V (Fig. 10(g)).

According to the Ragone plot (Fig. 10(h)), the energy density shows a relatively gradual variation trend with increasing power density. When the power density increases from 750 W kg^{-1} to 7499.88 W kg^{-1}, the energy density decreases from 31.44 Wh kg^{-1} to 12.7 Wh kg^{-1}, indicating that even with a significant increase in power density, the decrease in energy density remains relatively slow. Compared with the data reported in other literature, where activated carbon (AC) is used as a electrode to fabricate asymmetric capacitors, such as the AC//PPG-15 asymmetric supercapacitor device (24.65 Wh

kg^{-1} at 326.25 W kg^{-1}),[63] the Ni-MOF/rGO//AC asymmetric supercapacitor (17.13 Wh kg^{-1} at 750 W kg^{-1}),[64] and some supercapacitors with symmetrical electrodes, such as PMoW-PDDA-RGO//PMoW-PDDA-RGO (6.15 Wh kg^{-1} at 250 W kg^{-1}),[65] PAGH//PAGH (26.5 Wh kg^{-1} at 5135 W kg^{-1}),[66] NSeGA//NSeGA (26.3 Wh kg^{-1} at 900 W kg^{-1}),[67] the results indicate that {Mo_{132}}/rGA-6//{Mo_{132}}/rGA-6 has certain performance advantages. This outstanding rate capability can be attributed to the low internal resistance of the device system and the fast reaction kinetics of the electrode.

4. Conclusion

The introduction of pseudocapacitive polyoxometalate nanospheres {Mo_{132}}, combined with graphene's electric double-layer capacitive behavior, creates a synergistic effect that significantly enhances the material's electrochemical performance while moderately increasing its specific surface area. The specific surface areas of {Mo_{132}}/rGA-4, {Mo_{132}}/rGA-6, {Mo_{132}}/rGA-8, and pure rGA are 193.956 m^2 g^{-1}, 207.114 m^2 g^{-1}, 112.198 m^2 g^{-1} and 96.327 m^2 g^{-1}, respectively. The electrochemical performance of the three {Mo_{132}}/rGA composites was improved with varying degrees of improvement compared to that of pure rGA. CV tests revealed that {Mo_{132}}/rGA-4, {Mo_{132}}/rGA-6, and {Mo_{132}}/rGA-8 exhibited larger scan areas than pure rGA under identical testing conditions, indicating their enhanced charge storage capacity within the same voltage window and higher electrical conductivity. This conclusion was further corroborated by the EIS data, where the charge transfer resistances of the three {Mo_{132}}/rGA composites and pure rGA were found to be 2.385 Ω, 1.916 Ω, 2.578 Ω, and 2.861 Ω, respectively. The three {Mo_{132}}/rGA composites exhibited lower charge transfer resistance than pure rGA. Moreover, the degree of electrochemical improvement varied with the polyoxometalate content, with {Mo_{132}}/rGA-6 exhibiting superior performance compared to {Mo_{132}}/rGA-4, {Mo_{132}}/rGA-8, and pure rGA. The symmetric supercapacitor based on {Mo_{132}}/rGA-6 delivers a high energy density of 25 Wh kg^{-1} at a power density of 1490 W kg^{-1}. After 10 000 cycles at 10 A g^{-1}, the specific capacitance retention remains as high as 77.97%, with the coulombic efficiency approaching 100%.

Author contributions

Jihua Wang: writing – review & editing, supervision, methodology, and conceptualization. Renyou Huang: writing – original draft, methodology, investigation, and conceptualization. Junwang Liu: validation, data curation, and investigation. Xiaoyan Cai: validation, data curation, and investigation. Lige Gong: conceptualization and methodology. Limin Dong: conceptualization and methodology.

Conflicts of interest

The authors declare that they have no known competing financial interests or personal relationships that could have appeared to influence the work reported in this paper.

Data availability

The authors confirm that the data supporting the findings of this study are available within the article.

Acknowledgements

This study did not receive specific funding from the public, commercial, or non-profit sectors. We acknowledge Dr Yingyi Ma and Dr Weiwei Cui for valuable help in preparation of the manuscript.

References

1 C. Mu, Z. Du and W. Li, Taming of heteropoly acids into adhesive electrodes using amino acids for the development of flexible two-dimensional supercapacitors, *Polyoxometalates*, 2024, **3**(3), 9140062, DOI: 10.26599/pom.2024.9140062.
2 C. Shi, *et al.*, A host–guest compound formed by $Cu_3[P_2W_{18}O_{62}]$ and HKUST-1 with capacitance and H_2O_2 sensing properties, *Dalton Trans.*, 2023, **52**(27), 9406–9413, DOI: 10.1039/d3dt01205k.
3 Z. Al-Ghaus, A. Akbarinejad, *et al.*, Polyluminol–polyoxometalate hybrid hydrogels as flexible and soft supercapacitor electrodes, *J. Mater. Chem. A*, 2021, **9**(36), 20783–20793, DOI: 10.1039/d1ta05150d.
4 J. Choi, A. Jin, H. D. Jung, *et al.*, Nitrogen and sulfur co-doped graphene nanoribbons with well-ordered stepped edges for high-performance potassium-ion battery anodes, *Energy Storage Mater.*, 2022, **48**, 325–334, DOI: 10.1016/j.ensm.2022.03.041.
5 N. Wei, Y. Li, Y. Tang, *et al.*, Resilient bismuthene-graphene architecture for multifunctional energy storage and wearable ionic-type capacitive pressure sensor device, *J. Colloid Interface Sci.*, 2022, **626**, 23–34, DOI: 10.1016/j.jcis.2022.06.121.
6 M. B. Zheng, Y. Chi, Q. Hu, *et al.*, Carbon nanotube-based materials for lithium–sulfur batteries, *Mater. Chem. A*, 2019, **7**, 17204–17241, DOI: 10.1039/c9ta05347f.
7 N. Bahar and D. Ekinci, Dual capacitive behavior of hollow porous gold nanoparticle/multi-walled carbon nanotube composite films as anode and cathode electrode materials for supercapacitors, *J. Electron. Mater.*, 2024, **53**(3), 1476–1486, DOI: 10.1007/s11664-023-10874-0.
8 R. Liu, L. Wan, S. Liu, *et al.*, An interface-induced co-assembly approach towards ordered mesoporous carbon/graphene aerogel for high-performance supercapacitors, *Adv.*

Funct. Mater., 2014, **25**(4), 526–533, DOI: 10.1002/adfm.201570028.

9 Y. Cheng, L. Wu, C. Fang, *et al.*, Synthesis of porous carbon materials derived from laminaria japonica via simple carbonization and activation for supercapacitors, *J. Mater. Res. Technol.*, 2020, **9**(3), 3261–3271, DOI: 10.1016/j.jmrt.2020.01.022.

10 X. Wang, M. Barclay, R. Zhou, *et al.*, Graphene nanosheet-supported ultrafine RuO_2 quantum dots as electrochemical energy materials, *Mater. Today Sustain.*, 2024, **25**, 100646, DOI: 10.1016/j.mtsust.2023.100646.

11 R. Arunachalam, R. K. V. Prataap, R. R. Pavul, *et al.*, Pulse electrodeposited RuO_2 electrodes for high-performance supercapacitor applications, *Surf. Eng.*, 2018, **35**(2), 102–108, DOI: 10.1080/02670844.2018.1426408.

12 R. S. Kate, S. A. Khalate and R. J. Deokate, Overview of nanostructured metal oxides and pure nickel oxide (NiO) electrodes for supercapacitors: a review, *J. Alloys Compd.*, 2018, **734**, 89–111, DOI: 10.1016/j.jallcom.2017.10.262.

13 X. Q. Wang, W. T. Luo, Y. Q. Wang, *et al.*, Morphology-tuned synthesis of $MgCo_2O_4$@NiO arrays coated on nickel foam for high-rate supercapacitor electrode, *Electrochim. Acta*, 2023, **471**, 143279, DOI: 10.1016/j.electacta.2023.143279.

14 B. C. Liu, Z. S. Gao, Z. C. Yang, *et al.*, Flexible micro-supercapacitors fabricated from MnO_2 nanosheet/graphene composites with black phosphorus additive, *Prog. Nat. Sci.: Mater. Int.*, 2022, **32**, 10–19, DOI: 10.1016/j.pnsc.2021.10.008.

15 A. Zhang, R. Zhao, L. Hu, *et al.*, Adjusting the coordination environment of Mn enhances supercapacitor performance of MnO_2, *Adv. Energy Mater.*, 2021, **11**(32), 2101412, DOI: 10.1002/aenm.202101412.

16 P. Naska, A. Maiti, P. Chakraborty, *et al.*, Chemical supercapacitors: a review focusing on metallic compounds and conducting polymers, *Mater. Chem. A*, 2021, **9**, 1970–2017.

17 A. L. Pang, A. Arsad and M. Ahmadipour, Synthesis and factor affecting on the conductivity of polypyrrole: a short review, *Polym. Adv. Technol.*, 2021, **32**(4), 1428–1454, DOI: 10.1002/pat.5201.

18 S. Wang, Y. Liang, W. Zhuo, *et al.*, Freestanding polypyrrole/carbon nanotube electrodes with high mass loading for robust flexible supercapacitors, *Mater. Chem. Front.*, 2021, **5**(3), 1324–1329, DOI: 10.1039/D0QM00649A.

19 Y. Lin, H. Zhang, H. Liao, *et al.*, A physically crosslinked, self-healing hydrogel electrolyte for nano-wire PANI flexible supercapacitors, *Chem. Eng. J.*, 2019, **367**, 139–148, DOI: 10.1016/j.cej.2019.02.064.

20 Z. Sun, L. Zhao, H. Wan, *et al.*, Construction of polyaniline/carbon nanotubes-functionalized phase-change microcapsules for thermal management application of supercapacitors, *Chem. Eng. J.*, 2020, **396**, 125317, DOI: 10.1016/j.cej.2020.125317.

21 A. Alabadi, S. Razzaque, Z. Dong, *et al.*, Graphene oxide-polythiophene derivative hybrid nanosheet for enhancing performance of supercapacitor, *J. Power Sources*, 2016, **306**, 241–247, DOI: 10.1016/j.jpowsour.2015.12.028.

22 H. Vijeth, P. Ashokkumars, L. Yesappa, *et al.*, Flexible and high energy density solid-state asymmetric supercapacitor based on polythiophene nanocomposites and charcoal, *RSC Adv.*, 2018, **8**(55), 31414–31426, DOI: 10.1039/C8RA06102E.

23 Y. Chen, *et al.*, Polypyrrole-polyoxometalate/reduced graphene oxide ternary nanohybrids for flexible, all-solid-state supercapacitors, *Chem. Commun.*, 2015, **1 51**(62), 12377–12380, DOI: 10.1039/c5cc02717a.

24 S. Zhang, *et al.*, Simple and efficient polyoxomolybdate-mediated synthesis of novel graphene and metal nanohybrids for versatile applications, *J. Colloid Interface Sci.*, 2017, **514**, 507–516, DOI: 10.1016/j.jcis.2017.12.039.

25 Z. Qiu, Z. Liu, G. Wang, *et al.*, Highly redox-active oligomers between graphene sheets as ultrahigh capacitance/rate and stable electrodes for supercapacitors, *Energy Storage Mater.*, 2023, **60**, 102824, DOI: 10.1016/j.ensm.2023.102824.

26 D. Sun, X. Ni, D. Wang, *et al.*, The high-yield cutting conversion of porous graphene into graphene oxide quantum dots for boosting capacitive energy storage behavior, *Diamond Relat. Mater.*, 2022, **125**, 108979, DOI: 10.1016/j.diamond.2022.108979.

27 X. Yin, H. Li, L. Han, *et al.*, All Si_2N_4 nanowires membrane based high-performance flexible solid-tate asymmetric super-capacitor, *Small*, 2021, **17**(18), 2008056, DOI: 10.1002/smll.202008056.

28 X. Du, W. J. Jiang, L. Zu, *et al.*, Revisiting self-discharge of supercapacitors with multilayered graphene membrane as a model nanoporous electrode, *Energy Storage Mater.*, 2025, **74**, 103969, DOI: 10.1016/j.ensm.2024.103969.

29 Y. Lv, L. Ding, X. Wu, *et al.*, Coal-based 3D hierarchical porous carbon aerogels for high performance and super-long life supercapacitors, *Sci. Rep.*, 2020, **10**(1), 7022, DOI: 10.1038/s41598-020-64020-5.

30 L. Xia, X. Li, Y. Wu, *et al.*, Electrodes derived from carbon fiber-reinforced cellulose nanofiber/multiwalled carbon nanotube hybrid aerogels for high-energy flexible asymmetric supercapacitors, *Chem. Eng. J.*, 2020, **379**, 122325, DOI: 10.1016/j.cej.2019.122325.

31 S. Y. Lyu, H. J. Chang, L. F. Zhang, *et al.*, High specific surface area MXene/SWCNT/cellulose nanofiber aerogel film as an electrode for flexible supercapacitors, *Composites, Part B*, 2023, **264**, 110888, DOI: 10.1016/j.compositesb.2023.110888.

32 I. V. Anoshkin, J. Campion, D. V. Lioubtchenko, *et al.*, Freeze-drived carbon nanotube aerogels for high-frequency absorber applications, *ACS Appl. Mater. Interfaces*, 2018, **10**(23), 19806–19811, DOI: 10.1021/acsami.8b03983.

33 S. Liu, Y. Chen, P.-K. P. Dorsel, *et al.*, Facile preparation of nano-cellulose/multi-walled carbon nanotube/polyaniline composite aerogel electrodes with high area-specific capacitance for supercapacitors, *Int. J. Biol. Macromol.*, 2023, **238**, 124158, DOI: 10.1016/j.ijbiomac.2023.124158.

34 R. Chen, X. Li, Q. Huang, *et al.*, Self-assembled porous biomass carbon/RGO/nanocellulose hybrid aerogels for self-supporting supercapacitor electrodes, *Chem. Eng. J.*, 2021, **412**(4), 128755, DOI: 10.1016/j.cej.2021.128755.
35 S. Mukhopadhyay, J. Debgupta, C. Singh, *et al.*, A Keggin polyoxometalate shows water oxidation activity at neutral pH: POMS @ ZIF-8, an efficient and robust electrocatalyst, *Angew. Chem., Int. Ed.*, 2018, **57**(7), 1918–1923, DOI: 10.1002/ange.201711920.
36 W. Lu, *et al.*, Polyoxometalate-mediated confined self-assembly of sandwich-structured mesoporous polymer@rGO for high-performance aqueous zinc-iodine batteries, *Chem. Commun.*, 2025, **61**(69), 12908–12911, DOI: 10.1039/d5cc03153b.
37 G. Yang, *et al.*, Keggin-type polyoxometalate-based crown ether complex for lithium–sulfur batteries, *Chem. Commun.*, 2023, **59**(6), 788–791, DOI: 10.1039/d2cc05904e.
38 S. Li, *et al.*, A polyoxometalate-encapsulated nanocage cluster organic framework built from $\{Cu_4P_2\}$ units and its efficient bifunctional electrochemical performance, *Chem. Commun.*, 2025, **56**(96), 15177–15180, DOI: 10.1039/d0cc06665f.
39 Z. Sun, *et al.*, Synthesis of two new polyoxometalate-based organic complexes from 2D to 3D structures for improving supercapacitor performance, *Dalton Trans.*, 2025, **54**(15), 6093–6102, DOI: 10.1039/d5dt00284b.
40 G. Wang, *et al.*, A coordination polymer based on dinuclear (pyrazinyl tetrazolate) copper(II) cations and Wells–Dawson anions for high-performance supercapacitor electrodes, *Dalton Trans.*, 2017, **46**(40), 13897–13902, DOI: 10.1039/c7dt02230a.
41 B. Lu, *et al.*, pH-controlled assembly of five new organophosphorus Strandberg-type cluster-based coordination polymers for enhanced electrochemical capacitor performance, *Inorg. Chem.*, 2020, **59**(3), 1702–1714, DOI: 10.1021/acs.inorgchem.9b02858.
42 J. E. Madhusree, *et al.*, High-performance hybrid supercapacitor-immobilized Wells–Dawson polyoxometalates on activated carbon electrodes, *RSC Adv.*, 2023, **13**(38), 26744–26754, DOI: 10.1039/d3ra04478e.
43 W. H. Ho, T. Chen, K. Otake, *et al.*, Polyoxometalate adsorbed in a metal–organic framework for electrocatalytic dopamine oxidation, *Chem. Commun.*, 2020, **56**, 11763–11766, DOI: 10.1039/D0CC04904B.
44 F. Wang, L. Chen, H. L. Li, *et al.*, N-doped honeycomb-like porous carbon towards high-performance supercapacitor, *Chin. Chem. Lett.*, 2020, **31**, 1986–1990, DOI: 10.1016/j.cclet.2020.02.020.
45 C. Chen, M. K. Zhao, Y. Y. Cai, *et al.*, Scalable synthesis of strutted nitrogen doped hierarchical porous carbon nanosheets for supercapacitors with both high gravimetric and volumetric performances, *Carbon*, 2021, **179**, 458–468, DOI: 10.1016/j.carbon.2021.04.062.
46 H. M. Zhang, J. Y. Xue, S. Wang, *et al.*, Fabrication of high density and nitrogen-doped porous carbon for high volumetric performance supercapacitors, *J. Energy Storage*, 2022, **47**, 103657, DOI: 10.1016/j.est.2021.103657.
47 R. N. Nasim Khan, *et al.*, Pristine organo-imido polyoxometalates as an anode for lithium ion batteries, *RSC Adv.*, 2014, **4**(15), 7374, DOI: 10.1039/c3ra46645k.
48 L. Zhang, *et al.*, Improved supercapacitors and water splitting performances of Anderson-type manganese(III)–polyoxomolybdate through assembly with Zn-MOF in a host–guest structure, *J. Colloid Interface Sci.*, 2023, **654**(Pt B), 1393–1404, DOI: 10.1016/j.jcis.2023.10.136.
49 C. Li, N. Mizuno, K. Yamaguchi, *et al.*, Self-assembly of anionic polyoxometalate–organic architectures based on lacunary phosphomolybdates and pyridyl ligands, *J. Am. Chem. Soc.*, 2019, **141**(19), 7687–7692, DOI: 10.1021/jacs.9b02541.
50 A. Watanabe and J. Cai, Laser direct writing of conductive carbon microelectrodes and micro supercapacitor applications, *J. Laser Micro/Nanoeng.*, 2020, **15**(2), 92–96, DOI: 10.2961/jlmn.2020.02.2003.
51 N. Kumar, S.-B. Kim, S.-Y. Lee, *et al.*, Recent advanced supercapacitor: A review of storage mechanisms, electrode materials, modification, and perspectives, *Nanomaterials*, 2022, **12**(20), 3708, DOI: 10.3390/nano12203708.
52 S. Bashir, K. Hasan, M. Hina, *et al.*, Conducting polymer/graphene hydrogel electrodes based aqueous smart supercapacitors: A review and future prospects, *J. Electroanal. Chem.*, 2021, **898**, 115626, DOI: 10.1016/j.jelechem.2021.115626.
53 A. Müller, E. Krickemeyer, H. Bögge, *et al.*, Organizational forms of matter: An inorganic super fullerene and keplerate based on molybdenum oxide, *Angew. Chem., Int. Ed.*, 1998, **37**(24), 3359–3363, DOI: 10.1002/(SICI)1521-3773(19981231)37:24<3359::AID-ANIE3359>3.0.CO;2-J.
54 G. Mountrichas, S. Pispas, P. Aloukos, *et al.*, Aqueous dispersions of C60 fullerene by use of amphiphilic block copolymers: Preparation and nonlinear optical properties, *J. Phys. Chem. B*, 2007, **111**, 4315–4319, DOI: 10.1021/jp068796x.
55 M. Ichida, T. Sohda and A. Nakamura, Third-order nonlinear optical properties of C60 CT complexes with aromatic amines, *J. Phys. Chem. B*, 2000, **104**, 7082–7084, DOI: 10.1021/jp0009453.
56 D. Lu, *et al.*, A high performance solid-state asymmetric supercapacitor based on Anderson-type polyoxometalate-doped graphene aerogel, *Res. Chem. Intermed.*, 2019, **45**, 3237–3250, DOI: 10.1007/s11164-019-03789-1.
57 R. Li, *et al.*, Polyoxometalate-enabled photoreduction of graphene oxide to bioinspired nacre-like composite films for supercapacitor electrodes, *Composites, Part B*, 2017, **121**, 75–82, DOI: 10.1016/j.compositesb.2017.03.026.
58 Y. Liu, Y. Chen and W. Li, Synthesis of MOF derivatives@3D graphene hybrid materials towards high-performance electrode material for supercapacitors, *J. Mater. Sci.: Mater. Electron.*, 2022, **33**, 6514–6523, DOI: 10.1007/s10854-022-07826-5.

59 N. Saxena, *et al.*, One-pot synthesis of rGO/Ppy/Zn-MOF, ternary composite for high-performance supercapacitor application, *Chem. Phys. Lett.*, 2024, **856**, 141605, DOI: 10.1016/j.cplett.2024.141605.
60 N. Saxena, M. P. Bondarde, *et al.*, Electrochemical performance of graphene-oxide (GO) and MOF5-GO nanocomposite, *Ionics*, 2024, **30**, 8659–8672, DOI: 10.1007/s11581-024-05849-y.
61 M. Muhiuddin, *et al.*, Cost effective synthesis of sulfur and nitrogen co-doped graphene aerogel and application in binder free supercapacitor, *J. Appl. Phys.*, 2024, (3), 136, DOI: 10.1063/5.0202270.
62 J.-J. Han, C. Chen, *et al.*, Application of Cr-metal organic framework (MOF) modified polyaniline/graphene oxide materials in supercapacitors, *Ionics*, 2022, **28**, 2349–2362, DOI: 10.1007/s11581-022-04443-4.
63 J. Lin, S. Yan, X. Zhang, *et al.*, Facile preparation of holey Anderson-type polyoxometalate/polyaniline/graphene nanocomposites for supercapacitors, *Nano*, 2019, **14**(04), 1950049, DOI: 10.1142/s1793292019500498.
64 Y. Zhong, X. Cao, L. Ying, *et al.*, Homogeneous nickel metal–organic framework microspheres on reduced graphene oxide as novel electrode material for supercapacitors with outstanding performance, *J. Colloid Interface Sci.*, 2020, **561**, 265–274, DOI: 10.1016/j.jcis.2019.10.023.
65 Y. H. Ding, J. Peng, H. Y. Lu, *et al.*, Tungsten addenda mixed heteropolymolybdates supported on functionalized graphene for high-performance aqueous supercapacitors, *RSC Adv.*, 2016, **6**(84), 81085–81091, DOI: 10.1039/C6RA15381J.
66 X. Liu, S. Zou, K. Liu, *et al.*, Highly compressible three-dimensional graphene hydrogel for foldable all-solid-state supercapacitor, *J. Power Sources*, 2018, **384**, 214–222, DOI: 10.1016/j.jpowsour.2018.02.087.
67 J. Chen, C. Lin, M. Zhang, *et al.*, Constructing nitrogen, selenium co-doped graphene aerogel electrode materials for synergistically enhanced capacitive performance, *ChemElectroChem*, 2020, **7**(15), 3311–3318, DOI: 10.1002/celc.202000635.